

# Gaussian Process Priors for View-Aware Inference

Yuxin Hou\* Ari Heljakkka\* Arno Solin

Department of Computer Science  
Aalto University, Espoo, Finland

[firstname.lastname@aalto.fi](mailto:firstname.lastname@aalto.fi)

## Abstract

We derive a principled framework for encoding prior knowledge of information coupling between views or camera poses (translation and orientation) of a single scene. While deep neural networks have become the prominent solution to many tasks in computer vision, some important problems not so well suited for deep models have received less attention. These include uncertainty quantification, auxiliary data fusion, and real-time processing, which are instrumental for delivering practical methods with robust inference. While these are central goals in probabilistic machine learning, there is a tangible gap between the theory and practice of applying probabilistic methods to many modern vision problems. For this, we derive a novel parametric kernel (covariance function) in the pose space, SE(3), that encodes information about input pose relationships into larger models. We show how this soft-prior knowledge can be applied to improve performance on several real vision tasks, such as feature tracking, human face encoding, and view synthesis.

## 1. Introduction

Gaussian processes (GPs, [37]) provide a flexible probabilistic framework for combining *a priori* knowledge with forecasting, noise removal, and explaining data. Their strengths are in many ways complementary to those of deep neural networks which perform best in applications where large training data sets are available and the test points reside close to the training samples. The tremendous success of deep neural networks in solving many fundamental computer vision tasks has largely dictated the research in the past years, but recent interest in prediction under incomplete inputs has motivated combining the extreme flexibility and expressive power of current computer vision models with structured constraints encoded by GP priors. Application areas include uncertainty quantification (see discussion in [1, 26]), auxiliary data fusion, and prediction under scarce

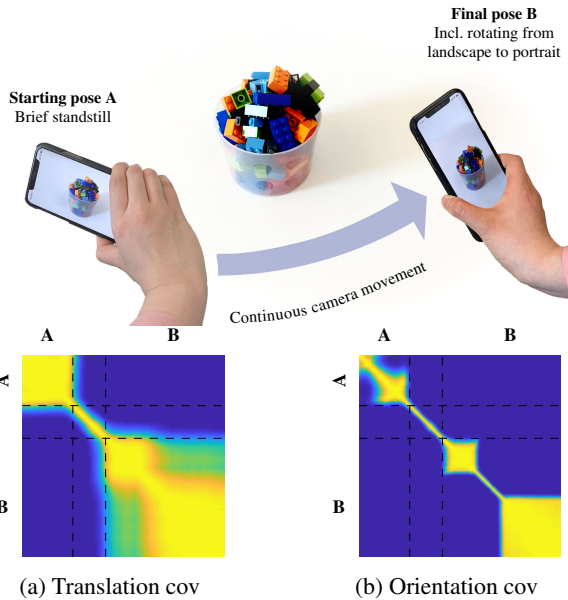


Figure 1. We propose a Gaussian process prior for encoding known six degrees-of-freedom camera movement (relative pose information) into probabilistic models. In this example, built-in visual-inertial tracking of the iPhone movement is used for pose estimation. The phone starts from standstill at the left and moves to the right (translation can be seen in the covariance in (a)). The phone then rotates from portrait to landscape which can be read from the orientation (view) covariance in (b).

data. These are instrumental for delivering practical methods and robustifying inference.

In this paper, we aim to fill a tangible gap between the theory and practice of applying probabilistic methods to certain computer vision tasks. We propose a tailored Gaussian process prior for encoding knowledge of camera poses (translation and orientation) into probabilistic models. In GPs, prior assumptions are encoded by a covariance function. As illustrated in Fig. 1 we aim to encode the notion of *similarity* of camera views given the known camera movement.

Visual odometry or egomotion refers to estimating the camera movement between frames. In practice, the estimation is typically fused with motion information from in-

\*Equal contribution

ertial sensors. New consumer hardware in smartphones and cars typically have these capabilities built-in—Apple iPhones/iPads run ARKit and Android devices Google AR-Core, both exposing real-time six degrees-of-freedom camera pose data. This readily available motion information could be utilized as priors for improving standard visual regression and classification tasks. However, typical computer vision methods operating on a stream of images consider the frames independently and merely post-process the outputs by, *e.g.*, linear interpolation or temporal low-pass filtering.

We propose a new (prior) model and stress its applicability as a building block in many future methods. The contributions of this paper are: (*i*) This paper is *bridging*: We emphasize the principled link between computer vision and non-parametric inference for encoding probabilistic information between the six degrees of freedom of a camera pose; (*ii*) We propose a new yet simple Gaussian process prior model (view covariance function) for encoding 3D camera orientation that extends the theory of GP models towards vision applications; (*iii*) We show how incorporating this prior can immediately facilitate several computer vision tasks, such as latent space interpolation, where we improve upon the state-of-the-art.

## 2. Background

Gaussian processes (GPs) provide a probabilistic plug-and-play framework for specifying prior knowledge inside models. As a general-purpose machine learning paradigm they are instrumental in applications for discovering structure in signals [9], regression tasks [2], data-efficient reinforcement learning [6], and probabilistic numerics [19]. In theory, their applicability is only limited by the availability of prior knowledge that can be encoded.

We focus on GP models [37] that admit the form of a *Gaussian process prior*  $f(\mathbf{x}) \sim \text{GP}(\mu(\mathbf{x}), \kappa(\mathbf{x}, \mathbf{x}'))$  and *likelihood*  $\mathbf{y} | \mathbf{f} \sim \prod_{i=1}^n p(y_i | f(\mathbf{x}_i))$ , where the data  $\mathcal{D} = \{(\mathbf{x}_i, y_i)\}_{i=1}^n$  are input–output pairs,  $\mu(\mathbf{x})$  the mean function, and  $\kappa(\mathbf{x}, \mathbf{x}')$  the covariance function of the GP prior. This family covers many standard modelling problems, including regression and classification tasks.

GPs are typically associated with two issues hindering their wider use: (*i*) prohibitive cubic scaling in the number of training samples  $n$  and (*ii*) the need for approximative inference when dealing with non-Gaussian likelihoods. From the perspective of computer vision, these limitations are central, but extensive research in the recent years has delivered methods to overcome these limitations by methods such as basis function projection [20, 30], matrix structure exploiting [43, 44], stochastic approximations [21, 27] and temporal models [38, 41]. The availability of GPU-accelerated software libraries such as GPflow [33] and GPyTorch [15] have recently made GP models more applicable as building blocks for larger models. Therefore, the traditional limitations are

getting less severe, allowing GPs to provide exciting opportunities for computer vision applications.

In this paper, the main contributions relate to the GP prior, where the *a priori* assumptions are encoded by the covariance function (kernel)  $\kappa(\cdot, \cdot)$ . Without loss of generality, we constrain our interest to models with  $\mu(\mathbf{x}) = 0$ . For computer vision and graphics applications, recent work in kernel design has focused more on encoding the ignorance rather than the knowledge about orientation. Invariant kernels (see, *e.g.*, [17]) can robustify deep convolutional models against rotation (rotation invariance), while translation insensitive kernels [8] can account for problems with patch similarity across images. We, however, aim to encode explicit prior knowledge about inter-image camera poses—view similarity—by crafting a view kernel that accounts for camera translation and orientation. This line of research has connections to distance measures between rigid bodies [34].

Perhaps due to the two limitations mentioned earlier, GPs have not been extensively used in computer vision applications. Sufficient and necessary conditions for Gaussian kernels on metric spaces are derived in [23], with the focus on theoretical ground-work. GP priors for rigid motions applied to object tracking is extensively studied in [28, 29], which also lays the ground for the comparisons in this paper. There has also been previous work in combining variational autoencoders with GP priors in vision [3, 10] and GP based latent variable models for multi-view and view-invariant facial expression recognition [11, 12]. In [3], GPs are applied to face image modelling, where the GP accounts for the pose, and in [42] they are used for 3D people tracking.

From an application point of view, leveraging information from consecutive views lies at the heart of many subfields in computer vision. Video analysis, multi-view methods, optical flow, visual tracking, and motion estimation and correction all directly build on the object or camera movement cues in consecutive image frames. View priors can also help in semantic processing of video [13] or depth estimation [22]. However, in many ‘one-shot’ applications in visual regression and classification, the frames of the image sequence are treated as independent of one another, and typically processed with linear interpolation or low-pass filtering.

## 3. Camera pose priors

In geometric computer vision (*e.g.*, [18]), the standard description of a camera projection model—relating the 3D world image points to the 2D camera image—is characterized by *extrinsic* and *intrinsic* camera parameters. The extrinsic parameters denote the coordinate system transformations from 3D world coordinates to 3D camera coordinates, while the intrinsic parameters map the 3D camera coordinates to image coordinates. In the standard *pinhole camera* model,

this corresponds to

$$(u \ v \ 1)^T \propto \mathbf{K} (\mathbf{R}^T \ -\mathbf{R}^T \mathbf{p}) (x \ y \ z \ 1)^T, \quad (1)$$

where  $(u, v)$  are the image (pixel) coordinates,  $(x, y, z) \in \mathbb{R}^3$  are the world coordinates,  $\mathbf{K}$  is the so-called camera matrix (intrinsic parameters) and the extrinsic parameters describe the position of the camera centre  $\mathbf{p} \in \mathbb{R}^3$ , and the camera orientation  $\mathbf{R}$  in world coordinates. From Eq. (1), given a set of fixed world coordinates and a known motion between frames the driver for changes in pixel values  $(u, v)$  is the camera pose  $P = \{\mathbf{p}, \mathbf{R}\}$ .

### 3.1. Kernels in SE(3)

In the mathematical sense, the three-dimensional camera poses belong to the special Euclidean group,  $\text{SE}(3)$ , whose elements are called rigid motions or Euclidean motions. They comprise arbitrary combinations of translations and rotations, but not reflections. This group contains affine transformations represented as a translation followed by a rotation:  $\text{SO}(3) \times \text{T}(3)$ , where the former denotes the special orthogonal rotation group and the latter the group of translations. A camera pose  $P = \{\mathbf{p}, \mathbf{R}\}$  is an element of this group. We consider a separable setup, where the orientation and translation contributions enter the prior in a separable manner:  $\kappa_{\text{pose}}(P, P') = \kappa_{\text{trans.}}(\mathbf{p}, \mathbf{p}') \kappa_{\text{view}}(\mathbf{R}, \mathbf{R}')$ . As the translation vectors reside in  $\mathbb{R}^3$ , we may directly write the translation kernel as any suitable covariance function (see, e.g., [9, 37] for overviews). An apparent first choice is the so-called squared exponential (RBF, exponentiated quadratic) covariance function:

$$\kappa(\mathbf{p}, \mathbf{p}') = \sigma^2 \exp\left(-\frac{\|\mathbf{p} - \mathbf{p}'\|^2}{2\ell^2}\right), \quad (2)$$

where  $\sigma^2$  denotes a magnitude and  $\ell > 0$  is a characteristic lengthscale hyperparameter. This particular choice of covariance function encodes continuity, smoothness, and translation invariance in  $\mathbf{p}$ . An example realization of the corresponding covariance matrix  $\mathbf{C}$ , for which  $C_{i,j} = \kappa_{\text{trans.}}(\mathbf{p}_i, \mathbf{p}_j)$ , is visualized in Fig. 1a.

### 3.2. View orientation kernels

Our interest is in formulating a proper view orientation covariance function. Here, the first choice could be to leverage the standard periodic kernel, which can be derived following MacKay [32]: Given a valid covariance function  $\kappa(\mathbf{u}, \mathbf{u}')$ , we can introduce a non-linear mapping  $\mathbf{x} \mapsto \mathbf{u}(\mathbf{x})$ , through which to define a new covariance function  $\kappa'(\mathbf{x}, \mathbf{x}') \triangleq \kappa(\mathbf{u}(\mathbf{x}), \mathbf{u}(\mathbf{x}'))$ . The standard periodic kernel (c.f., [37]) is usually derived by the mapping  $\theta \mapsto \mathbf{u}$  that warps  $\theta$  to the unit circle:  $\mathbf{u}(\theta) = (\cos(\theta), \sin(\theta))$ .

Combining this with the covariance function in Eq. (2) gives

$$\begin{aligned} \kappa(\theta, \theta') &= \exp\left(-\frac{\|\mathbf{u}(\theta) - \mathbf{u}(\theta')\|^2}{2\ell^2}\right) \\ &= \exp\left(-\frac{2\sin^2((\theta - \theta')/2)}{\ell^2}\right), \end{aligned} \quad (3)$$

which can be used for imposing a periodic prior over inputs  $\theta \in \mathbb{R}$ . Now, Eq. (3) could be extended to the space of arbitrary three-dimensional rotations by assuming the three view rotation (Euler) angles  $\boldsymbol{\theta} = (\theta_1, \theta_2, \theta_3)$  to be fully separable. This would correspond to a separable view kernel (Fig. 2d):

$$\kappa(\boldsymbol{\theta}, \boldsymbol{\theta}') = \prod_{j=\{1,2,3\}} \exp\left(-\frac{2\sin^2((\theta_j - \theta'_j)/2)}{\ell_j^2}\right). \quad (4)$$

This, however, has several issues related to the use of Euler angles. For three-dimensional rotations Euler angles suffer from possibly singular representations and gimbal lock (loss of one degree of freedom, see, e.g., [7, 14]), and should thus be avoided as an internal representation of orientation.

**Quaternion formalism** Instead of Euler angles common representations for orientation are given in terms of rotation matrices or quaternions. The set of unit quaternions,  $\mathbf{q} = (q_w, q_x, q_y, q_z)$ , s.t.  $\|\mathbf{q}\| \equiv 1$ , forms the 3D rotation group  $\text{SO}(3)$  (the group of  $3 \times 3$  rotation matrices) covering the  $S^3$  sphere. For defining a distance metric similar to that of the norm of warping in Eq. (3), the apparent first choice is the arc distance. The geodesic (arc) distance  $d_g(\mathbf{q}_1, \mathbf{q}_2)$  between unit quaternions  $\mathbf{q}_1$  and  $\mathbf{q}_2$  along the surface of the  $S^3$  sphere is defined as  $d_g(\mathbf{q}_1, \mathbf{q}_2) = \|\ln(\mathbf{q}_1^{-1} \mathbf{q}_2)\|$  (see, e.g., [35]). The geodesic distance (or the corresponding arc angle) can be computed by explicitly expanding the quaternion logarithm via the quaternion dot product:

$$d_g(\mathbf{q}_1, \mathbf{q}_2) = \arccos(2(\mathbf{q}_1 \cdot \mathbf{q}_2)^2 - 1). \quad (5)$$

In order to seek a similar, but higher-dimensional, form of Eq. (3), the quaternion representation can directly be used as a mapping. This would make sense, as the derivation of the standard periodic covariance function can be viewed as a mapping onto the complex plane and quaternions represent a 4D extension of complex numbers. We may define the distance between quaternions  $\mathbf{q}_1$  and  $\mathbf{q}_2$  as the norm of their difference,  $d_{\text{quat}}(\mathbf{q}_1, \mathbf{q}_2) = 2\|\mathbf{q}_1 - \mathbf{q}_2\|$ . In quaternion algebra, this still translates to the Euclidean norm of element-wise differences. The quaternion model has been discussed in previous work by Lang *et al.* [28, 29].

However, the resulting covariance function is not well-behaved in all orientations—due to non-uniqueness of quaternions—as can be seen from the plot in Fig. 2b (or the plots in the Appendix), where full-turn ( $2\pi$ ) correlations are zero.

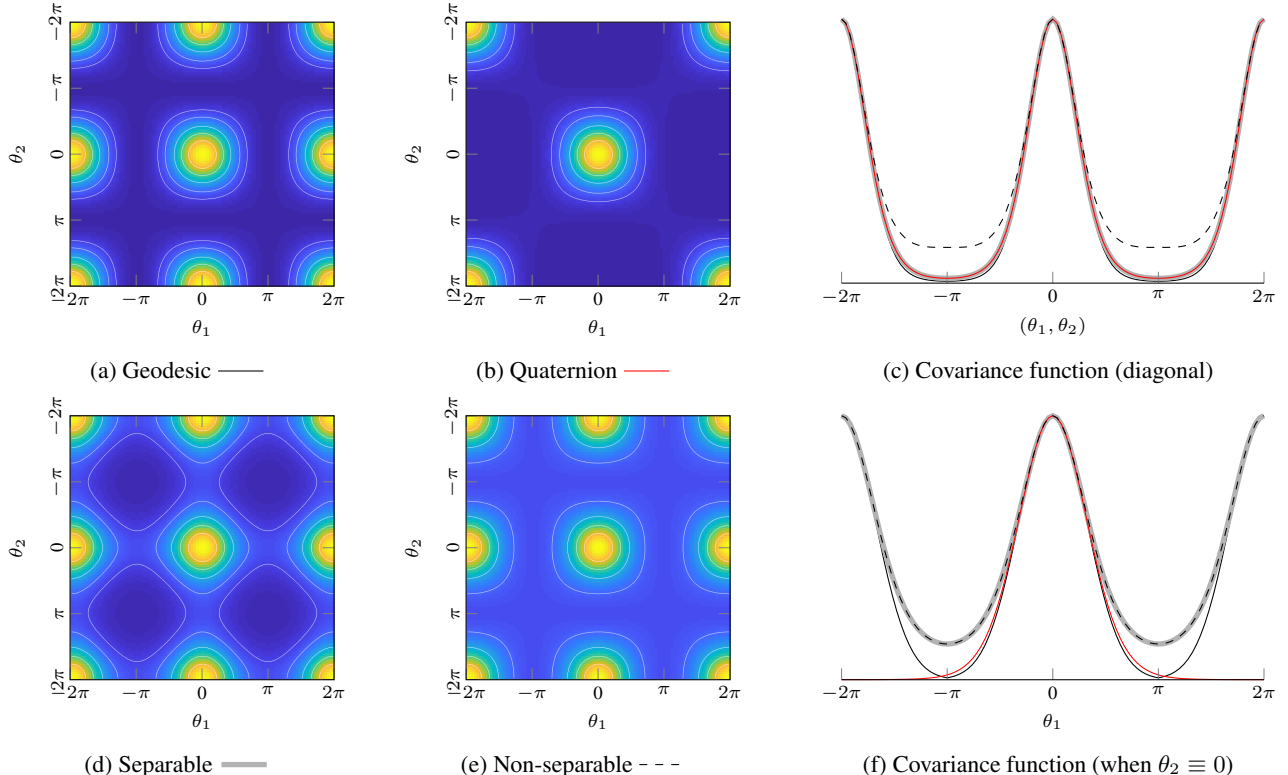


Figure 2. (**Left**) Covariance function between two degrees-of-freedom rotations (for simpler visualization) with scale 0 — 1 and  $\ell = 1$ . (a) uses the geodesic distance, (b) the quaternion norm distance, (d) shows the separable periodic covariance function, and (e) the proposed non-separable covariance function. (**Right**) Cross-sections along the diagonal and  $\theta_2 \equiv 0$ , showing that in 1D (d) and (e) coincide, while (e) is symmetric in 2D/3D.

**Rotation matrix formalism** The peculiarities with the previous formulations, as visualized in Fig. 2, acted as a motivation to seek a more principled generalization of the periodic covariance function to general rotations. As for quaternions in the previous section, the geodesic distance between two orientations defined by rotation matrices  $\mathbf{R}_1$  and  $\mathbf{R}_2$  can be defined through the arccosine of the matrix trace operator (see Appendix A.1):  $d_g(\mathbf{R}_1, \mathbf{R}_2) = \arccos\left(\frac{1}{2}(\text{tr}(\mathbf{R}_1^\top \mathbf{R}_2) - 1)\right)$ , which is equal to the distance metric in quaternion space in Eq. (5) (visualized in Fig. 7a in the Appendix). A Taylor expansion (see Appendix A.2) for this distance metric around the origin gives a mapping that we use for the non-separable covariance function (visualized in Fig. 2e):

$$\kappa_{\text{view}}(\mathbf{R}, \mathbf{R}') = \exp\left(-\frac{\text{tr}(\mathbf{I} - \mathbf{R}^\top \mathbf{R}')}{2\ell^2}\right). \quad (6)$$

To account for different characteristic scaling per axis, Eq. (6) may be generalized to  $\kappa_{\text{view}}(\mathbf{R}, \mathbf{R}') = \exp(-\frac{1}{2}\text{tr}(\boldsymbol{\Lambda} - \mathbf{R}^\top \boldsymbol{\Lambda} \mathbf{R}'))$ , where  $\boldsymbol{\Lambda} = \text{diag}(\ell_x^{-2}, \ell_y^{-2}, \ell_z^{-2})$  (NB: The  $\ell$ s are coupled and its interpretation is not as straightforward as scaling for the respective axes). The proposed 3D view kernel in Eq. (6) gives the standard periodic kernel as a special case (see Fig. 2f and Appendix A.3).

To summarize, we propose the non-sparable orientation covariance function  $\kappa_{\text{view}}(\cdot, \cdot)$  that preserves a symmetric correlation structure around origin (like the geodesic model), does not suffer from the degeneracy of Euler angles, and returns the standard periodic kernel as a special case in 1D.

## 4. Application experiments

In the experiments, we show examples of three real-world applications of the view kernel. The first experiment focuses on quantifying the practical differences in the different view priors from the previous section. The second experiment focuses on view synthesis in a challenging GPPVAE model, where the model has been extended with the general view prior. The third experiment is concerned with latent space interpolation for human face modelling which showcases the general applicability of the view information.

### 4.1. Comparison of camera motion kernels

In the first experiment, we compare different GP priors for filling in visual feature tracks. The motivation of these experiments is not the application itself (feature-track interpolation), but evaluating the flexibility and capability of the proposed methods to capture real-world camera motion.

Table 1. RMSE and NLPD measures for the feature tracking example for predicting pixel coordinates in interleaved frames based on the Google Tango device motion. Results calculated over 533 tracks of handheld movement. **Smaller is better.**

Model (kernel) description	RMSE	NLPD
Translation only	8.01	3.679
Separable orientation only [32]	15.38	4.187
Non-separable orientation only (ours)	15.23	4.179
Linear-in-extrinsics [28]	12.24	3.940
Trans. & sep. orientation	7.66	3.631
Trans. & non-sep. orientation (ours)	<b>7.57</b>	<b>3.616</b>

The data (sequence *01* from [5]) contains handheld motion of a Google Tango device while walking in a shopping mall. It comprises a video file with 789 frames (over the time-course of 4:20 min, resolution  $640 \times 480$ ) and associated three-dimensional camera pose information for every frame. We apply a Shi–Tomasi feature extractor [39] to select strong corner points in the frames and track them across frames by a pyramidal Lucas–Kanade tracker [31]. Example feature track histories are shown in Fig. 3. We discard short tracks and are left with 533 full-length feature tracks, tracked over 20 frames each, giving input–output pairs(iv)  $\{(P_i, (u, v)_i)\}_{i=1}^{20}$ , where  $(u, v)$  are the pixel coordinates and  $P_i$  denotes the camera pose. In each track, we use 85% of the points for training and 15% for testing.

We set up a GP regression task for predicting the  $u$  and  $v$  coordinates for unseen frames along the track. Because the world coordinates points are regarded fixed, the point locations in the frames are driven by the movement of the camera (*c.f.*, Eq. (1)). We consider independent GP regression models for every track  $j = 1, 2, \dots, 533$  in  $u$  and  $v$ :  $u_i^{(j)} = f_u^{(j)}(P_i^{(j)}) + \varepsilon_{u,i}^{(j)}$  and  $v_i^{(j)} = f_v^{(j)}(P_i^{(j)}) + \varepsilon_{v,i}^{(j)}$  with GP priors  $f_u^{(j)} \sim \text{GP}(0, \kappa(P, P'))$  and  $f_v^{(j)} \sim \text{GP}(0, \kappa(P, P'))$ .

We consider six different movement-induced GP priors: (i) only translation (Eq. (2)), (ii) the separable periodic kernel by using Euler angles (Eq. (4) as based on [32]), (iii) the proposed non-separable orientation kernel (Eq. (6)), (iv) a linear-in-extrinsics kernel as a baseline (see Sec. 3.3 in [28]), and (v–vi) product kernels between the translation kernel and each orientation kernel. For each covariance function, we jointly learn the hyperparameters of the GP priors (the noise and magnitude scales and the lengthscales are considered shared) by maximizing w.r.t. log likelihood.

We evaluate the models on the test data in terms of predictive RMSE and negative log-predictive density (NLPD). The results in Table 1 show the proposed non-separable view orientation kernel outperforms the separable orientation kernel. The first three methods only use either the translation or orientation input, while the last three use the full 6-DoF

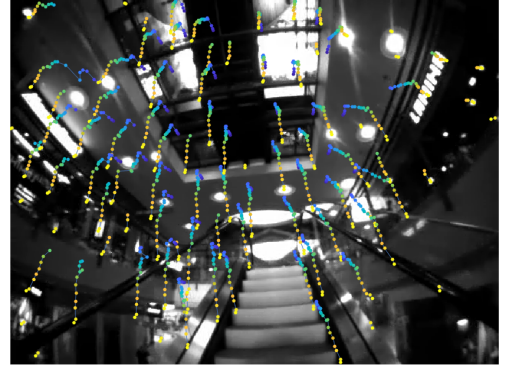


Figure 3. Example feature tracks for one frame from the Tango device with natural motion to fill in.

pose as inputs. The results show that neither camera rotation nor translation can alone provide good regressors for the task. Also, just trying to use the camera extrinsic matrix directly (without leveraging knowledge of the manifold the extrinsics live in) does not suffice. Finally, we see that our non-separable model provides a clear benefit over simply disregarding the link between 3D orientations.

## 4.2. View synthesis with a Gaussian process prior variational autoencoder

We consider an experiment where we use the Gaussian Process Prior Variational Autoencoder (GPPVAE) by Casale *et al.* [3] to predict unseen views of objects. The GPPVAE attempts to capture correlations in both object identities and views by leveraging covariance structure in latent space. However, in the original paper, the experiments only considered a rotation in one dimension (modelled with the standard periodic kernel). As our proposed kernel function can work with arbitrary poses, it can be plugged into the GPPVAE model to account for three-dimensional views. Using the model of Casale *et al.* [3], given training images  $\mathcal{Y}$ , object feature vectors  $\mathcal{X}$ , and training views  $\mathcal{P}$ , the predictive posterior for an image  $\mathbf{y}_*$  for an object with features  $\mathbf{x}_*$  seen from a camera pose  $P_*$  is given by

$$p(\mathbf{y}_* | \mathbf{x}_*, \mathcal{Y}, \mathcal{X}, \mathcal{P}) \approx \int \underbrace{p(\mathbf{y}_* | \mathbf{z}_*)}_{\text{decode prediction}} \underbrace{p(\mathbf{z}_* | \mathbf{x}_*, P_*, \mathcal{Z}, \mathcal{X}, \mathcal{P})}_{\text{GP predictive posterior}} \underbrace{q(\mathcal{Z} | \mathcal{Y})}_{\text{encode training data}} d\mathbf{z}_* d\mathcal{Z}. \quad (7)$$

We carried out an experiment with ShapeNet [4] 3D chair models at  $128 \times 128$  resolution. There are 6778 different chair shapes in total. For each object, we render images from 18 fixed views, considering both azimuth angles ( $0^\circ, 60^\circ, \dots, 300^\circ$ ) and elevation angles ( $0^\circ, 45^\circ, -45^\circ$ ). The camera view angles are shown in Fig. 4a. We randomly selected 80% images for training (97,603 images), 10% for validation (12,201 images) and 10% for testing (12,200 images).

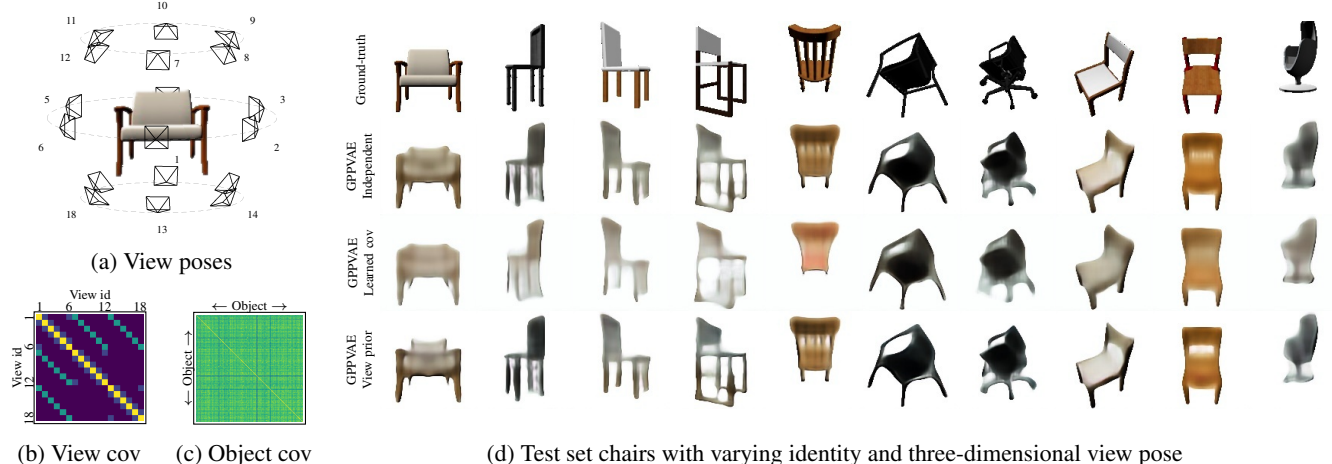


Figure 4. Results from experiments on the PoseNet chairs data set. (a) Visualization of the 18 camera view angles considered in the data. (b–c) View and object covariances resulting from GPPVAE jointly learning the object features and hyperparameters. (d) Comparison of out-of-sample predictions of chairs in out-of-sample views, where the proposed view prior delivers sharper predictive samples.

The task is to predict chair images  $\mathbf{y}_*$  in orientations  $P_*$  =  $\mathbf{R}_*$  that are unobserved. Unlike many approaches to similar tasks, we do not learn any 3D representation explicitly. As our sampled views are located on the same sphere, we do not consider translation between cameras. For the object covariance, we use a linear kernel between learned object features. The resulting composite kernel  $\kappa(\mathbf{x}, \mathbf{R}; \mathbf{x}', \mathbf{R}')$  expresses the covariance between two chair images in terms of the relative view orientation between view orientations  $\mathbf{R}$  and  $\mathbf{R}'$  and object feature vectors  $\mathbf{x}$  and  $\mathbf{x}'$ :

$$\kappa(\mathbf{x}, \mathbf{R}; \mathbf{x}', \mathbf{R}') = \underbrace{\mathbf{x}^\top \mathbf{x}'}_{\text{object}} \underbrace{\exp\left(-\frac{1}{2}\text{tr}(\Lambda - \mathbf{R}^\top \Lambda \mathbf{R}')\right)}_{\text{view}}. \quad (8)$$

We learn the lengthscale hyperparameters  $\ell_x, \ell_y, \ell_z$  as part of the training. For the most part, we replicate the setup as presented in [3], but due to rich variability in chair shapes, we consider a higher rank ( $M = 128$ ) for the object covariance (see Appendix C for details).

Fig. 4 shows results for the chair view synthesis experiment. The object and view covariances are shown in Figs. 4b and 4c (view covariance matrix is in log-scale due to characteristic lengthscales being  $\sim 5.3^\circ$ ). For the proposed view kernel, the MSE is  $0.024 \pm 0.013$ , which has better performance than using a pose-independent prior ( $0.026 \pm 0.014$ ) or learning the full view-covariance matrix as in [3] ( $0.062 \pm 0.041$ ). Compared to the face experiment in [3], the chairs were harder to model. When attempting to learn the full view covariance matrix, GPPVAE had problems disentangling the contribution of view and object, which shows as inferior performance compared to the view prior in Eq. (8). Moreover, models with an independent or fully-learned covariance matrix cannot be generalized to novel views without retraining, while our proposed kernel can be evaluated for arbitrary new views.

### 4.3. Robust interpolation for face reconstruction

As a final experiment, we consider view-aware GP interpolation in the latent space of a Generative Adversarial Network (GAN, [16]) for face generation. We use the GAN as a feature extractor, and do GP regression in the latent space representations. The data comprises short video sequences of faces of four volunteers captured by an Apple iPhone XS. We used a tailored application for capturing the videos stream ( $1440 \times 1920$  at 60 Hz) interleaved with camera poses from the Apple ARKit API which uses the phone camera and motion sensors for returning high-frequency camera poses.

In absence of a built-in encoder, as in case of many GANs, we can use an optimization process to find out the best latent code for an image  $j$ . The traditional approach has been to learn these codes from i.i.d. training data, and under the assumption that we essentially have only a single ‘observation’ of each entity that the image represents. We now relax this assumption and consider the more general case where we postulate the existence of a ‘hidden’ latent code  $\mathbf{f}_j \in \mathbb{R}^d$  for certain invariant elements of an input sample (such as face identity), and re-interpret the latent code produced by an encoder or optimizer as a noisy ‘observation’  $\mathbf{y}_j \in \mathbb{R}^d$  of the correct code.

Furthermore, we consider the situation where we have multiple images that share those invariant elements (such as the same face identity viewed from different angles) and thereby we have, correspondingly, multiple ‘observations’ of the correct latent code that corresponds to those invariant elements. We can now cast this as a GP regression problem, where each latent dimension,  $i = 1, 2, \dots, d$  is considered independently. The likelihood is  $y_{j,i} = f_i(P_j) + \varepsilon_{j,i}$ ,  $\varepsilon_{j,i} \sim N(0, \sigma_n^2)$ , for frames  $j = 1, 2, \dots, n$ . The GP prior is over the camera poses  $P_j$ :  $f_i(P) \sim GP(0, \kappa_{\text{view}}(P, P'))$ .

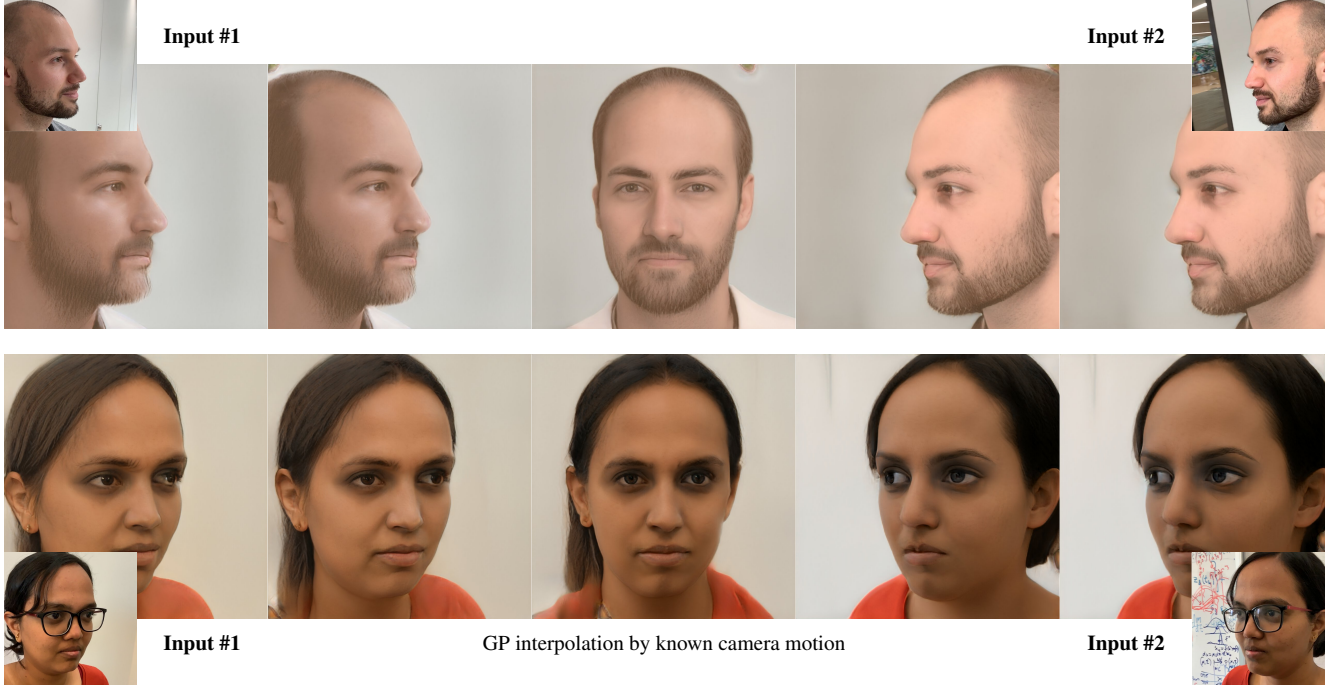


Figure 5. Two examples of view-aware latent space interpolation using the latent space of StyleGAN [24]. These reconstructions are based on only taking the first and the last frame of short side-to-side video sequences (Input #1 and #2), encoding them into the GAN latent space, and interpolating the intermediate frames using only the information of the associated camera poses (from Apple ARKit) captured on an iPhone XS. The intermediate frames were recovered by regressing the latent space with our view-aware GP prior. The frames are re-created in correct head orientations. The irregular angular speed of the camera movement (not shown) is precisely captured by our method, resulting in non-symmetric interpolations. **See supplementary material for video examples.**

Solving these independent GP regression problems only requires inverting one  $n \times n$  covariance matrix, which makes inference fast.

GP inference can be directly employed in two different scenarios: noise reduction and view synthesis. For the first one, given several images of the same object, we can use the encoder or optimizer to find the corresponding latent code. The problem is that if our assumption is correct and these codes can actually be characterized as noisy observations, when we decode the codes back to individual images, we should observe that they are inconsistent. The issue may not be clear when visually examining single frames, but it is plain when the frames are combined into a video (see the Supplement for video examples).

Utilizing the view kernel and a sequence of images with the viewing orientation information, we can predict the expected latent code,  $E[\mathbf{f}(P_j) | \mathcal{D}]$ , for each image. We can apply these predictions in several ways. First, we can take the sequence of latent codes that correspond to the images and effectively de-noise the latent code of each frame. When we represent those reconstructed sequential images as video, the effect is to make the video smoother and with reduced artifacts.

In the second scenario, we can take only a subset of the

frames, in some cases even a single start and single end frame (see Fig. 5), and interpolate the rest of the frames in the latent space *according to the camera movement* by predicting the latent codes,  $E[\mathbf{f}(P_*) | \mathcal{D}]$ , for unseen views  $P_*$ . In contrast to linear interpolation in the latent space, this approach actually follows the original camera movement and therefore can reproduce the same angles as the original camera run (see Fig. 6 for comparison of this effect).

We demonstrate this approach in the latent space of StyleGAN [24] on different face identities (see Fig. 5 and the supplement for more examples). We find the latent codes of the start and end images using an optimizer, leveraging VGG16 feature projections [36, 40]. The optimization happens in the  $18 \times 512$  latent space. The latent codes of the images between them are predicted by our method and then decoded back to  $1024 \times 1024$  image space with the generator network of the GAN. The values for the three hyperparameters were fixed to  $\sigma^2 = 0.1$ ,  $\ell = 1.098$ , and  $\sigma_n^2 = 0.0001$ . Even if the GAN encoding produced stable results, the considerable slowness of finding the latent codes by optimization (in range of minutes for single image) motivates the present approach, as we now need to encode only a small subset of frames and match the camera movement by the GP prediction.

**Fig. 5** shows two examples of view-aware interpolation

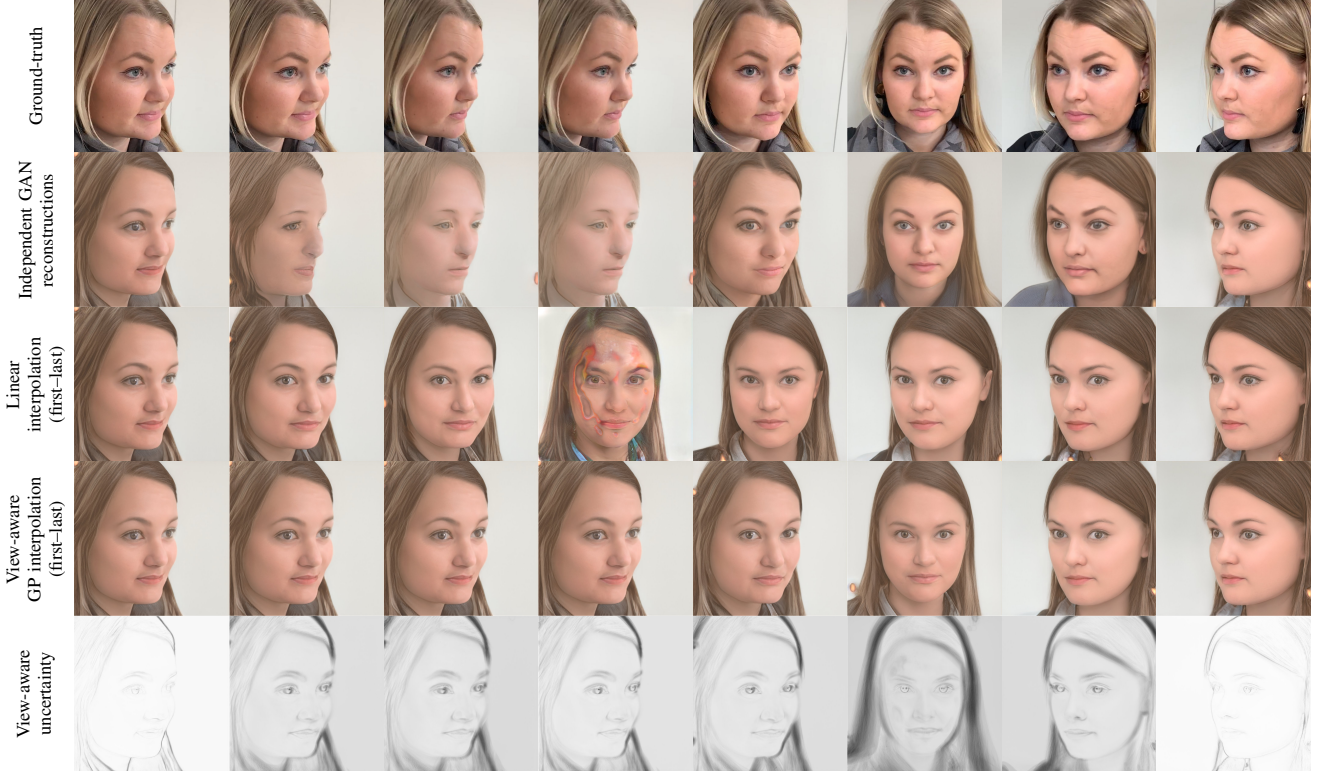


Figure 6. Row #1: Frames separated by equal time intervals from a camera run, aligned on the face. Row #2: Each frame independently projected to GAN latent space and reconstructed. Row #3: Frames produced by reconstructing the first and the last frame and linearly interpolating the intermediate frames in GAN latent space. Row #4: Frames produced by reconstructing the first and the last frame, but interpolating the intermediate frames in GAN latent space by our view-aware GP prior. It can be seen that although linear interpolation achieves good quality, the azimuth rotation angle of the face is lost, as expected. With the view-aware prior, the rotation angle is better preserved. Row #5: The per-pixel uncertainty visualized in the form of standard deviation of the prediction at the corresponding time step. Heavier shading indicates higher uncertainty around the mean trajectory.

with only a start and end frame given as inputs and the interpolation conditioned on the known camera movement trajectory. In Fig. 6, we compare to independent frame-by-frame reconstructions, partly of low quality due to the limits of reconstructing challenging input head poses with StyleGAN (leading to slight variation in face alignment). As a baseline, we also linearly interpolate between the first and last frame, which (for apparent reasons) fails to capture the varying camera motion, with mismatches in the head angle. The GP solution with our view prior smoothly matches the view orientation by simultaneously maintaining the features of the face identity. Furthermore, we visualize the frame-wise marginal uncertainty (posterior variance  $V[\mathbf{f}(P_j) | \mathcal{D}]$ ) of the GP predictions as a standard deviation map in image space. We calculate the maps by drawing 100 samples from the posterior process and calculating the standard deviation over faces. The uncertainty is small in the beginning/end (where the inputs are) and highest towards the part where even the linear interpolation is most off—showing the practical uncertainty quantification capabilities of the model.

## 5. Discussion and conclusion

We have presented a new view-aware approach (covariance function model) to encode *a priori* knowledge about camera movement into computer vision tasks. We consider this view kernel if not the missing piece, at least an important building block, for applying Gaussian process priors to many computer vision models. The covariance function itself is simple, yet elegant, and circumvents possible problems related to degeneracy and gimbal lock if applying alternative approaches. Furthermore, the model includes the standard periodic covariance function as a special case.

To underline the practical importance of our work, we considered three different real-world applications for the proposed model. Our quantitative experiments in Secs. 4.1 and 4.2 showed that the view prior can encode authentic movement and provide a soft-prior for view synthesis. In the final example (Sec. 4.3), we showed how the model can be of direct practical value by acting as a camera-motion-aware interpolator. Videos and material related to the paper is available on <https://aaltoml.github.io/view-aware-inference>.

## Acknowledgments

We thank Jaakko Lehtinen and Janne Hellsten (NVIDIA) for the StyleGAN latent space projection script and advice on its usage. Authors acknowledge funding from GenMind Ltd.

## References

- [1] Charles Blundell, Julien Cornebise, Koray Kavukcuoglu, and Daan Wierstra. Weight uncertainty in neural network. In *Proceedings of the 32nd International Conference on Machine Learning (ICML)*, volume 37 of *Proceedings of Machine Learning Research*, pages 1613–1622. PMLR, 2015.
- [2] Thang Bui, Daniel Hernández-Lobato, Jose Hernández-Lobato, Yingzhen Li, and Richard Turner. Deep Gaussian processes for regression using approximate expectation propagation. 48:1472–1481, 2016.
- [3] Francesco Paolo Casale, Adrian Dalca, Luca Saglietti, Jennifer Listgarten, and Nicolo Fusi. Gaussian process prior variational autoencoders. In *Advances in Neural Information Processing Systems (NeurIPS)*, pages 10369–10380. Curran Associates, Inc., 2018.
- [4] Angel Xuan Chang, Thomas A. Funkhouser, Leonidas J. Guibas, Pat Hanrahan, Qi-Xing Huang, Zimo Li, Silvio Savarese, Manolis Savva, Shuran Song, Hao Su, Jianxiong Xiao, Li Yi, and Fisher Yu. ShapeNet: An information-rich 3D model repository. *arXiv preprint arXiv:1512.03012*, 2015.
- [5] Santiago Cortés, Arno Solin, Esa Rahtu, and Juho Kannala. ADVIO: An authentic dataset for visual-inertial odometry. In *Proceedings of the European Conference on Computer Vision (ECCV)*, pages 419–434, 2018.
- [6] Marc P Deisenroth and Carl E Rasmussen. PILCO: A model-based and data-efficient approach to policy search. pages 465–472. Omnipress, 2011.
- [7] James Diebel. Representing attitude: Euler angles, unit quaternions, and rotation vectors. *Matrix*, 58(15–16):1–35, 2006.
- [8] Vincent Dutordoir, Mark van der Wilk, Artem Artemev, Marcin Tomczak, and James Hensman. Translation insensitivity for deep convolutional Gaussian processes. *arXiv preprint arXiv:1902.05888*, 2019.
- [9] David Duvenaud. *Automatic Model Construction with Gaussian Processes*. PhD thesis, Computational and Biological Learning Laboratory, University of Cambridge, Cambridge, UK, 2014.
- [10] Stefanos Eleftheriadis, Ognjen Rudovic, Marc Peter Deisenroth, and Maja Pantic. Variational Gaussian process auto-encoder for ordinal prediction of facial action units. In *Asian Conference on Computer Vision (ACCV)*, pages 154–170. Springer, 2016.
- [11] Stefanos Eleftheriadis, Ognjen Rudovic, and Maja Pantic. Discriminative shared Gaussian processes for multiview and view-invariant facial expression recognition. *IEEE Transactions on Image Processing*, 24(1):189–204, 2015.
- [12] Stefanos Eleftheriadis, Ognjen Rudovic, and Maja Pantic. Multi-conditional latent variable model for joint facial action unit detection. In *IEEE International Conference on Computer Vision (ICCV)*, pages 3792–3800, 2015.
- [13] Mark Everingham, Josef Sivic, and Andrew Zisserman. “Hello! My name is... Buffy”—Automatic naming of characters in TV video. In *British Machine Vision Conference (BMVC)*, volume 2, page 6, 2006.
- [14] Roy Featherstone. *Rigid Body Dynamics Algorithms*. Springer, New York, 2014.
- [15] Jacob Gardner, Geoff Pleiss, Kilian Q Weinberger, David Bindel, and Andrew G Wilson. GPyTorch: Blackbox matrix-matrix Gaussian process inference with GPU acceleration. In *Advances in Neural Information Processing Systems (NeurIPS)*, pages 7576–7586. Curran Associates, Inc., 2018.
- [16] Ian Goodfellow, Jean Pouget-Abadie, Mehdi Mirza, Bing Xu, David Warde-Farley, Sherjil Ozair, Aaron Courville, and Yoshua Bengio. Generative adversarial nets. In *Advances in Neural Information Processing Systems (NIPS)*, pages 2672–2680, 2014.
- [17] Bernard Haasdonk and Hans Burkhardt. Invariant kernel functions for pattern analysis and machine learning. *Machine Learning*, 68(1):35–61, 2007.
- [18] Richard Hartley and Andrew Zisserman. *Multiple View Geometry in Computer Vision*. Cambridge University Press, Cambridge, UK, 2003.
- [19] Philipp Hennig, Michael A Osborne, and Mark Girolami. Probabilistic numerics and uncertainty in computations. *Proceedings of the Royal Society of London A: Mathematical, Physical and Engineering Sciences*, 471(2179), 2015.
- [20] James Hensman, Nicolas Durrande, and Arno Solin. Variational Fourier features for Gaussian processes. *Journal of Machine Learning Research (JMLR)*, 18(151):1–52, 2018.
- [21] James Hensman, Nicolò Fusi, and Neil D. Lawrence. Gaussian processes for big data. In *Uncertainty in Artificial Intelligence (UAI)*, pages 282–290. AUAI Press, 2013.
- [22] Yuxin Hou, Juho Kannala, and Arno Solin. Multi-view stereo by temporal nonparametric fusion. In *IEEE International Conference on Computer Vision (ICCV)*, pages 2651–2660, 2019.
- [23] Sadeep Jayasumana, Richard Hartley, Mathieu Salzmann, Hongdong Li, and Mehrtash Harandi. Kernel methods on the Riemannian manifold of symmetric positive definite matrices. In *Proceedings of the IEEE Conference on Computer Vision and Pattern Recognition (CVPR)*, pages 73–80, 2013.
- [24] Tero Karras, Samuli Laine, and Timo Aila. A style-based generator architecture for generative adversarial networks. In *IEEE Conference on Computer Vision and Pattern Recognition (CVPR)*, 2019.
- [25] Vahid Kazemi and Josephine Sullivan. One millisecond face alignment with an ensemble of regression trees. In *IEEE Conference on Computer Vision and Pattern Recognition (CVPR)*, pages 1867–1874, 2015.
- [26] Alex Kendall and Yarin Gal. What uncertainties do we need in Bayesian deep learning for computer vision? In *Advances in Neural Information Processing Systems (NIPS)*, pages 5574–5584. 2017.
- [27] Karl Krauth, Edwin V Bonilla, Kurt Cutajar, and Maurizio Filippone. AutoGP: Exploring the capabilities and limitations of Gaussian process models. In *Uncertainty in Artificial Intelligence (UAI)*. AUAI Press, 2017.
- [28] Muriel Lang and Sandra Hirche. Computationally efficient rigid-body gaussian process for motion dynamics. *IEEE Robotics and Automation Letters*, 2(3):1601–1608, 2017.

- [29] Muriel Lang, Martin Kleinsteuber, and Sandra Hirche. Gaussian process for 6-DoF rigid motions. *Autonomous Robots*, 42(6):1151–1167, 2018.
- [30] Miguel Lázaro-Gredilla, Joaquín Quiñonero-Candela, Carl E. Rasmussen, and Aníbal R. Figueiras-Vidal. Sparse spectrum Gaussian process regression. *Journal of Machine Learning Research (JMLR)*, 11:1865–1881, Jun 2010.
- [31] Bruce D. Lucas and Takeo Kanade. An iterative image registration technique with an application to stereo vision. In *International Conference on Artificial Intelligence (IJCAI)*, pages 674–679. Vancouver, BC, Canada, 1981.
- [32] David JC MacKay. Introduction to Gaussian processes. *NATO ASI Series F Computer and Systems Sciences*, 168:133–166, 1998.
- [33] Alexander G de G Matthews, Mark van der Wilk, Tom Nickson, Keisuke Fujii, Alexis Boukouvalas, Pablo León-Villagrá, Zoubin Ghahramani, and James Hensman. GPflow: A Gaussian process library using TensorFlow. *Journal of Machine Learning Research (JMLR)*, 18(1):1299–1304, 2017.
- [34] Claudio Mazzotti, Nicola Sancisi, and Vincenzo Parenti-Castelli. A measure of the distance between two rigid-body poses based on the use of platonic solids. In *ROMANSY 21-Robot Design, Dynamics and Control*, pages 81–89. Springer, 2016.
- [35] Frank C Park and Bahram Ravani. Smooth invariant interpolation of rotations. *ACM Transactions on Graphics*, 16(3):277–295, 1997.
- [36] Puzer (GitHub user). StyleGAN encoder – Converts real images to latent space. <https://github.com/Puzer/stylegan-encoder>, 2019. GitHub repository.
- [37] C. E. Rasmussen and C. K. I. Williams. *Gaussian Processes for Machine Learning*. The MIT Press, 2006.
- [38] Simo Särkkä, Arno Solin, and Jouni Hartikainen. Spatiotemporal learning via infinite-dimensional Bayesian filtering and smoothing. *IEEE Signal Processing Magazine*, 30(4):51–61, 2013.
- [39] Jianbo Shi and Carlo Tomasi. Good features to track. In *Proceedings of the IEEE Computer Society Conference on Computer Vision and Pattern Recognition (CVPR)*, pages 593–600, 1994.
- [40] Karen Simonyan and Andrew Zisserman. Very deep convolutional networks for large-scale image recognition. In *International Conference on Learning Representations (ICLR)*, 2015.
- [41] Arno Solin, James Hensman, and Richard E Turner. Infinite-horizon Gaussian processes. In *Advances in Neural Information Processing Systems (NeurIPS)*, pages 3486–3495. Curran Associates, Inc., 2018.
- [42] Raquel Urtasun, David J Fleet, and Pascal Fua. 3D people tracking with Gaussian process dynamical models. In *IEEE Conference on Computer Vision and Pattern Recognition (CVPR)*, pages 238–245, 2006.
- [43] Ke Alexander Wang, Geoff Pleiss, Jacob R Gardner, Stephen Tyree, Kilian Q Weinberger, and Andrew Gordon Wilson. Exact Gaussian processes on a million data points. *arXiv preprint arXiv:1903.08114*, 2019.
- [44] Andrew Gordon Wilson and Hannes Nickisch. Kernel interpolation for scalable structured Gaussian processes (KISS-GP). In *International Conference on Machine Learning (ICML)*, volume 37 of *PMLR*, pages 1775–1784, 2015.

---

# Supplementary Material for Gaussian Process Priors for View-Aware Inference

---

This file holds the supplementary material for ‘Gaussian Process Priors for View-Aware Inference’. We provide further details on the derivations, experiment setups, additional results, and details on the video supplements.

## A. Derivations

### A.1. Derivation of the geodesic distance

The geodesic arc distance along the  $S^3$  sphere defined by a rotation  $\mathbf{R} \in SO(3)$  can be intuitively derived from the following linear algebraic and trigonometric identities. Consider the eigendecomposition of  $\mathbf{R}$  where the eigenvectors define the rotation axis and the eigenvalues define the angle (or ‘distance’). The eigenvalues of a rotation matrix come as a complex conjugate pair and ‘1’. This can be represented as  $\{1, e^{\pm i\theta}\}$ , where  $\theta$  is the rotation angle or arc distance.

In order to solve  $\theta$  given  $\mathbf{R}$ , recall the definition of cosine in terms of complex numbers:

$$\cos \theta = \frac{1}{2} (e^{i\theta} + e^{-i\theta}). \quad (9)$$

The trace of a matrix equals the sum of its eigenvalues, and using the definition of cosine form above, we recover:

$$\text{tr}(\mathbf{R}) = 1 + e^{i\theta} + e^{-i\theta} = 1 + 2 \cos \theta. \quad (10)$$

Solving for  $\theta$  gives

$$\theta = \arccos\left(\frac{\text{tr}(\mathbf{R}) - 1}{2}\right). \quad (11)$$

The relative rotation between two orientations  $\mathbf{R}_1, \mathbf{R}_2 \in SO(3)$  is given by  $\mathbf{R}_1^\top \mathbf{R}_2$ , thus we recover the geodesic distance metric that was used in Sec. 3.2 in the main paper:

$$d_g(\mathbf{R}_1, \mathbf{R}_2) = \arccos\left(\frac{\text{tr}(\mathbf{R}_1^\top \mathbf{R}_2) - 1}{2}\right). \quad (12)$$

### A.2. Derivation of the three-dimensional view kernel

We seek to derive the 3D counterpart of the standard periodic kernel. For this we set up a local approximation around the origin for the geodesic distance. Recall that the Taylor series of cosine:

$$\cos \theta = 1 - \frac{1}{2}\theta^2 + \frac{1}{4!}\theta^4 + \dots \quad (13)$$

Truncating after the second term gives  $\cos \theta \approx 1 - \frac{1}{2}\theta^2$ . Substituting  $\sqrt{2\alpha}$  for  $\theta$  yields  $\cos \sqrt{2\alpha} \approx 1 - \alpha$ . Thus we get the local approximation

$$\arccos(1 - \alpha) \approx \sqrt{2\alpha}. \quad (14)$$

Applying the above to the geodesic distance in Eq. (12), and substituting  $\alpha$  for  $\frac{1}{2}(3 - \text{tr}(\mathbf{R}_1^\top \mathbf{R}_2))$ , we get

$$d_g(\mathbf{R}_1, \mathbf{R}_2) \approx \sqrt{2\alpha} = \sqrt{3 - \text{tr}(\mathbf{R}_1^\top \mathbf{R}_2)} = \sqrt{\text{tr}(\mathbf{I} - \mathbf{R}_1^\top \mathbf{R}_2)}, \quad (15)$$

which we label the ‘view’ distance

$$d_{\text{view}}(\mathbf{R}_1, \mathbf{R}_2) = \sqrt{\text{tr}(\mathbf{I} - \mathbf{R}_1^\top \mathbf{R}_2)}. \quad (16)$$

As was seen in the main paper, this approximation is accurate around origin (see Fig. 7e).

### A.3. Link between the standard periodic kernel and the 3D view kernel

We define a general rotation matrix  $\mathbf{R}$  with respect to yaw, pitch, and roll defined through rotations around the axes,  $x$ ,  $y$ , and  $z$ , respectively:

$$\mathbf{R}_x(\theta) = \begin{pmatrix} 1 & 0 & 0 \\ 0 & \cos \theta & -\sin \theta \\ 0 & \sin \theta & \cos \theta \end{pmatrix}, \quad (17)$$

$$\mathbf{R}_y(\theta) = \begin{pmatrix} \cos \theta & 0 & \sin \theta \\ 0 & 1 & 0 \\ -\sin \theta & 0 & \cos \theta \end{pmatrix}, \text{ and} \quad (18)$$

$$\mathbf{R}_z(\theta) = \begin{pmatrix} \cos \theta & -\sin \theta & 0 \\ \sin \theta & \cos \theta & 0 \\ 0 & 0 & 1 \end{pmatrix}. \quad (19)$$

Thus a rotation around the axes can be given by Euler angles  $\boldsymbol{\theta} = (\theta_1, \theta_2, \theta_3)$ :  $\mathbf{R}(\boldsymbol{\theta}) = \mathbf{R}_z(\theta_3) \mathbf{R}_y(\theta_2) \mathbf{R}_x(\theta_1)$ .

Taking the trace term from Eq. (16), we can parametrize the rotations in terms of  $\boldsymbol{\theta}$  and  $\boldsymbol{\theta}'$ , giving:

$$\text{tr}(\mathbf{I} - \mathbf{R}(\boldsymbol{\theta})^\top \mathbf{R}(\boldsymbol{\theta}')). \quad (20)$$

In the degenerate case where there is only rotation around one of the axes (say  $\theta_1 = \theta'_1$  and  $\theta_2 = \theta'_2$ ,  $\theta_3 = \theta$  and  $\theta'_3 = \theta'$ ), we get

$$\text{tr}(\mathbf{I} - \mathbf{R}_z(\theta)^\top \mathbf{R}_z(\theta')). \quad (21)$$

Expanding the product and summing up the diagonal elements gives

$$(1 - \cos(\theta - \theta')) + (1 - \cos(\theta - \theta')) + 0 = 2 - 2 \cos(\theta - \theta'). \quad (22)$$

By applying the half-angle formula ( $\sin^2(\frac{1}{2}\alpha) = \frac{1}{2}(1 - \cos\alpha)$ ), we recover

$$4 \sin^2\left(\frac{\theta - \theta'}{2}\right), \quad (23)$$

which is exactly the form of the squared norm warping in the standard periodic covariance function [32, 37]:  $\|\mathbf{u}(\theta) - \mathbf{u}(\theta')\|^2$  for  $\mathbf{u}(\theta) = (\cos\theta, \sin\theta)$ . The above derivation can be repeated for any of the angles  $\{\theta_1, \theta_2, \theta_3\}$ , showing that in the case of rotation only around one axis, the proposed view covariance function coincides with the standard periodic covariance function.

## B. Details on the feature tracking experiment

[Fig. 8](#) shows the pose covariance matrix for all the 789 frames in the video by considering both translation and rotation of the camera (the ‘Trans. & non-sep. orientation’ in [Table 1](#)). The prior covariance used for each track is thus a subset of the whole covariance matrix, as all feature tracks share the same hyperparameters. After optimizing w.r.t. log likelihood, we get the values of hyperparameters as follows: magnitude scale  $\sigma^2 = 36.4$ , lengthscale  $\ell = 0.962$ , and noise scale  $\sigma_n^2 = 53.6$ . Before regression, for the training points in each track, we subtract the mean of the track so that each track will have zero mean, and we add the mean back after regression. [Fig. 9](#) shows GP regression results of three tracks and the prior pose covariance in each respective case. For each trajectory, there are three randomly chosen missing points, and we predict the  $u$  and  $v$  pixel coordinates for the missing points separately by using the same pose kernel in the GP prior. The red points corresponds to original data points, where ‘+’ indicates training points and ‘●’ corresponds to unseen test points. The blue line is the GP posterior mean.

As an additional supplementary file, we include a video showing the full feature tracks used in the experiment in [Sec. 4.1](#). The feature histories are colour-coded so that the cool colours represent feature point locations in the past.

## C. Details on the view synthesis experiment

In the experiments in [Sec. 4.2](#), we used a similar setup as in GPPVAE with joint optimization (GPPVAE-joint) in [3], where we first train the standard VAE and then optimize the autoencoder and GP parameters jointly. For the VAE model, the dimension of the latent space is  $L = 256$  and the convolutional architecture is the same as in [3]. For the object kernel, we set the dimensionality of the object feature

vectors to  $M = 128$ . For the view kernel, we follow the [Eq. \(8\)](#), where the lengthscale hyperparameters  $\ell_x, \ell_y, \ell_z$  in the diagonal matrix  $\Lambda$  are learned during training. The whole model is implemented in PyTorch. The standard VAE was trained with 1000 epochs and the GP parameters were trained jointly for 290 epochs with batch size of 64 on a desktop workstation (NVIDIA GTX 1080 Ti, i7-7820X CPU, and 63 GB memory). For each of the models, the training time was around one day.

## D. Details on the face reconstruction experiment

For the experiments in [Sec. 4.3](#), we started from recording a single MPEG movie file for each face identity, 20–30 seconds each, with associated camera poses (from Apple ARKit) captured on an iPhone XS. We decomposed the movie into a sequence of single image frames that we crop to  $1024 \times 1024$  and aligned the detected faces therein using the approach of [24] based on [25]. For each image, we then created the corresponding StyleGAN [24] latent representation using a script based on [36], as follows. We first generated a corresponding initial ‘guess’ values for the  $18 \times 512$  latent variable matrix that StyleGAN generator uses to produce a  $1024 \times 1024$  image. We fed both the generated image and the real camera image to a pre-trained VGG-16 [40] network. We read off the VGG-16 feature space representations of both images, and used the difference as a loss to drive an optimization process that, upon convergence, produces the latent variable value that can be used to reproduce an image that closely resembles the original camera image. The StyleGAN model was pre-trained on the FFHQ dataset of [24]. The projections were implemented in Tensorflow while the GP part was implemented in PyTorch.

This rather heuristic projection process is very slow (60–120 seconds per image on a Titan V GPU), but usually produces high quality images (while other generative models with built-in encoders could have produced results 50–100 times faster, but typically lower quality) with only occasional visible artifacts. The weaknesses of the model can be seen when failing to properly reconstruct face shots where the azimuth rotation angle is large. We run the reconstruction process for every fifth frame of the original video. Some small segments of some of the videos were excluded from beginning or end when the reconstruction failed completely.

We then carried out three experiments. First, we used the latent codes of all reconstructed images (total of 50–200 frames, depending on original video length and face identity) to construct a single matrix comprising all the training samples. We then ran the GP regression on the matrix in the usual manner using our view-aware prior, and the camera pose data from the original video frames. This resulted in a reconstructed latent variable matrix of the same size as before. We then fed these latent variables back to StyleGAN

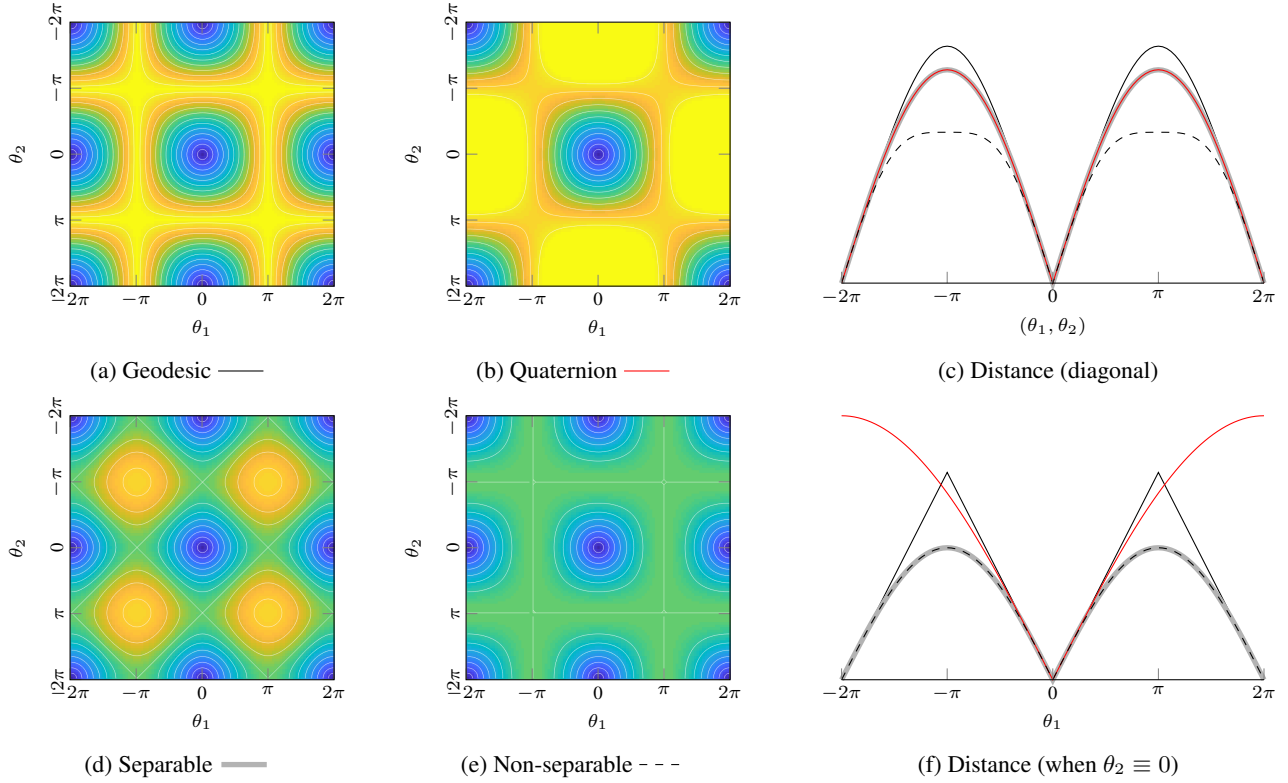


Figure 7. **(Left)** Distance matrices between two degrees-of-freedom rotations (for simpler visualization) with scale 0 [color bar]  $\pi$ . (a) shows the geodesic distance, (b) the quaternion norm distance, (c) the separable periodic distance, and (e) the non-separable orientation distance. **(Right)** Distance evaluations along the diagonal and when  $\theta_2 \equiv 0$ .

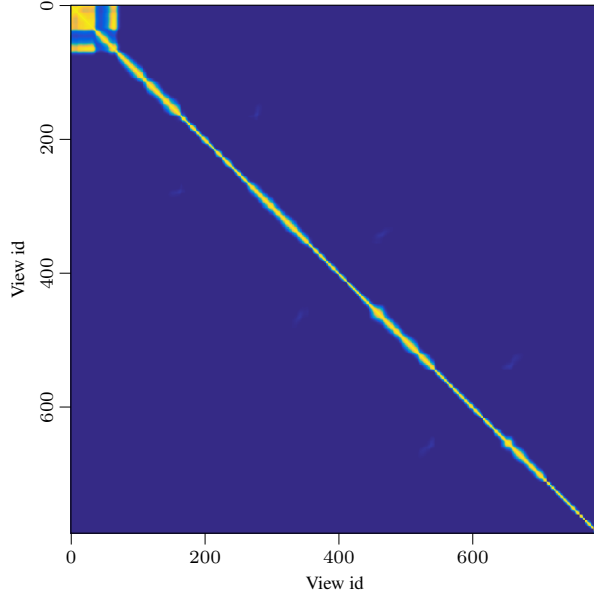
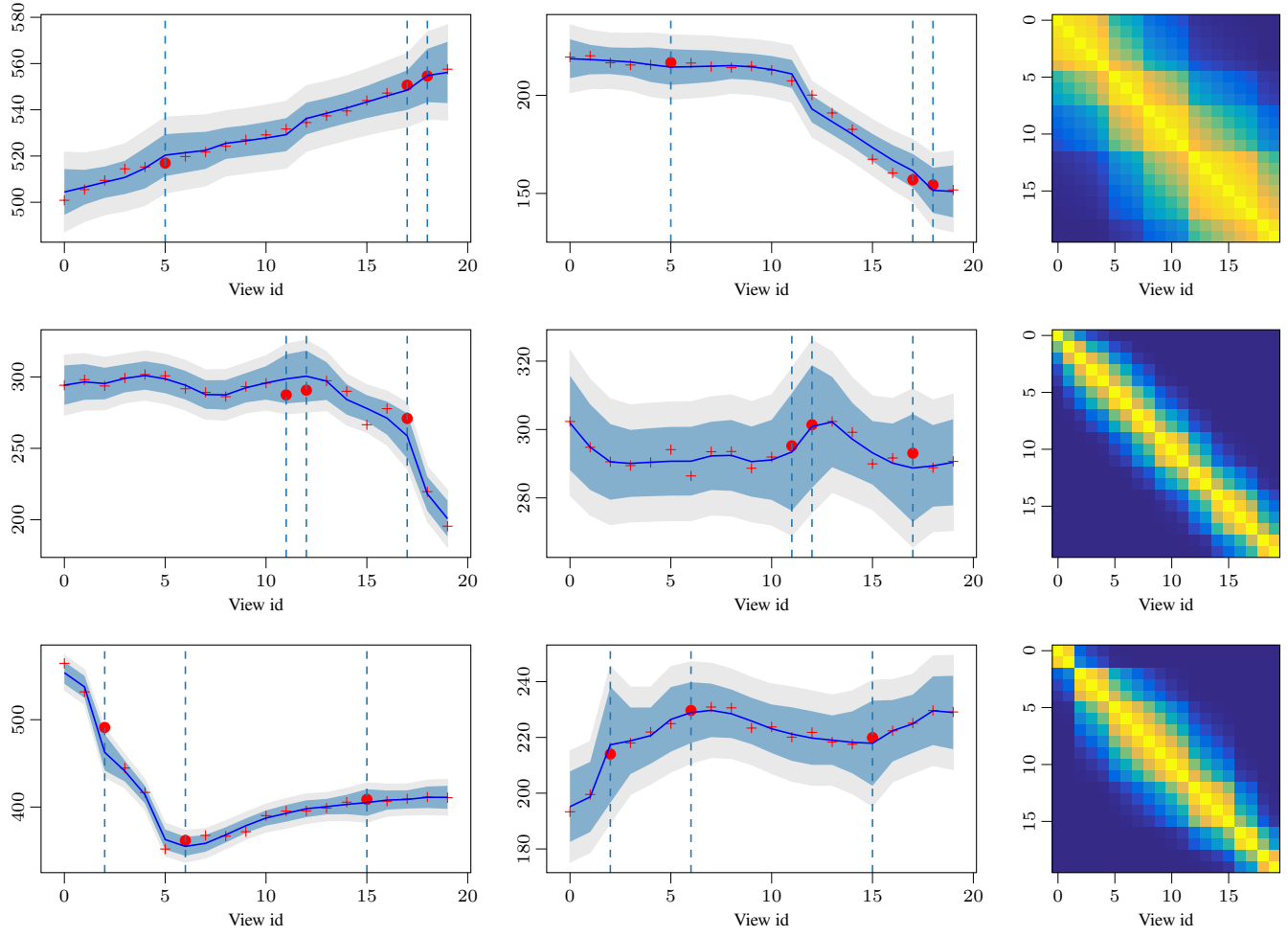


Figure 8. Pose covariance matrix for all the 789 frames in the video in the tracking experiment in Sec. 4.1.

and decoded each code back to the image space, resulting in smoothed versions of each of the original frames. The smoothing effect can be seen in the attached video.

Second, we set up an essentially similar experiment, but now using the latent codes of no more than the start and end frames (*i.e.*, two frames only, resulting in  $2 \times 18 \times 512$



(a) GP regression of  $u$  coordinates

(b) GP regression of  $v$  coordinates

(c) Pose covariance

Figure 9. GP regression results of three tracks (out of 533) using the pose kernel in Sec. 4.1. The red points corresponds to ground-truth trajectories, where ‘+’ means training points and ‘●’ corresponds to unseen points. The blue points are predicted mean values. The shaded patches denote the 95% quantiles.

latent matrix) of the sequence, in combination with the full covariance matrix of the camera pose. Nonetheless, we used the same method as above to reproduce the whole sequence of latent codes (*e.g.*,  $50 \times 18 \times 512$ ). That is, all the latent variables between the start and end frames were interpolated with the view-aware GP prior. Again, we fed the resulting latent codes back to StyleGAN, and confirmed that the resulting frames not only have high quality, but also follow the camera movement (see Fig. 5 and Fig. 10).

Finally, to evaluate the specific contribution of the view-aware GP prior, we tried a simpler experiment where the same start and end frames were used as an input, but the intermediate latent codes were produced by simple linear interpolation in the latent space (*i.e.*, just taking latent values from evenly sized intervals between the two known latent values). We again fed these to StyleGAN to produce the

corresponding images. As should be expected (if the latent space is well-behaved), the resulting images still have high quality, but they simply rotate the face in evenly sized increments per frame. This should be contrasted with the previous experiment with view-aware prior, in which the frames actually match the original camera movement. For comparison, see Fig. 6.

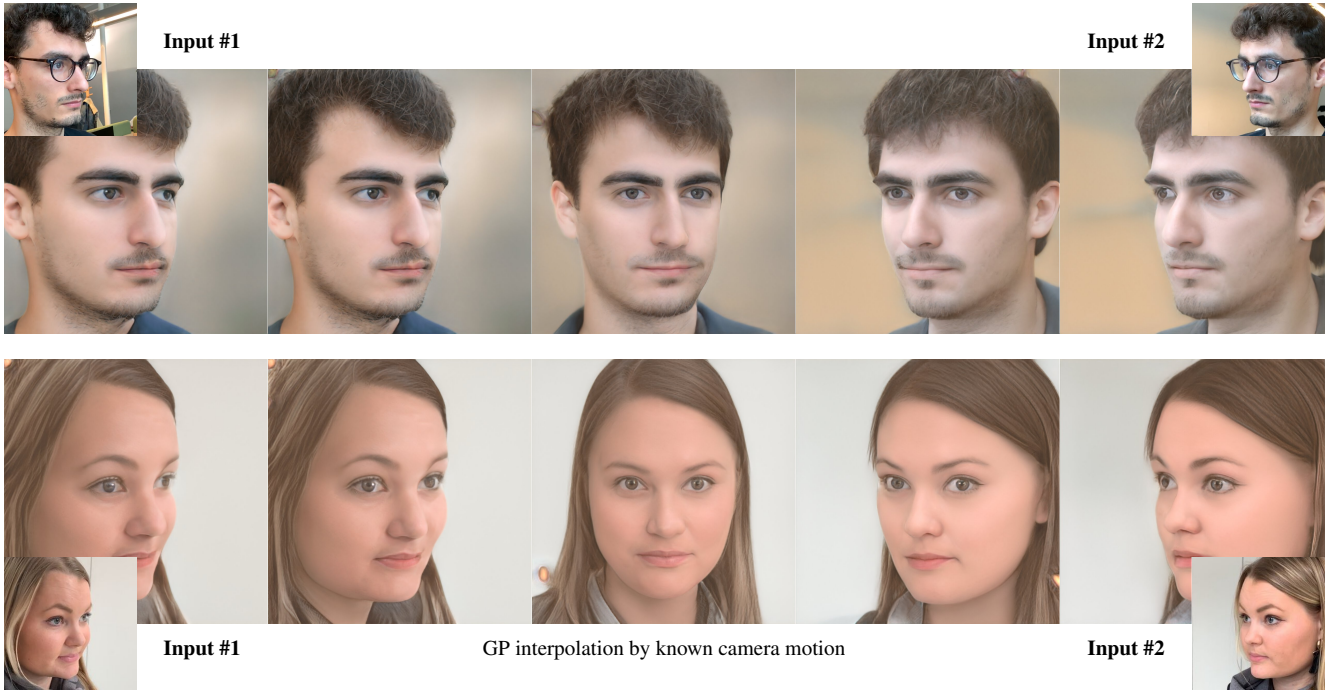


Figure 10. Two more examples of view-aware latent space interpolation using the latent space of StyleGAN [24]. These reconstructions are based on only taking the first and the last frame of short side-to-side video sequences (Input #1 and #2), encoding them into the GAN latent space, and interpolating the intermediate frames using only the information of the associated camera poses (from Apple ARKit) captured on an iPhone XS. The intermediate frames were recovered by regressing the latent space with our view-aware GP prior. The frames are re-created in correct head orientations. The irregular angular speed of the camera movement (not shown) is precisely captured by our method, resulting in non-symmetric interpolation.